LETTER • OPEN ACCESS

What goes in must come out: the oceanic outgassing of anthropogenic carbon

To cite this article: Damien Couespel and Jerry Tjiputra 2024 *Environ. Res. Lett.* **19** 014086

View the article online for updates and enhancements.

ENVIRONMENTAL RESEARCH
LETTERS

LETTER

What goes in must come out: the oceanic outgassing of anthropogenic carbon

Damien Couespel[*] and Jerry Tjiputra

NORCE Norwegian Research Centre AS, Bjerknes Centre for Climate Research, Bergen, Norway
* Author to whom any correspondence should be addressed.

E-mail: daco@norceresearch.no

Abstract

About 25% of the emitted anthropogenic CO_2 is absorbed by the ocean and transported to the interior through key gateways, such as the Southern Ocean or the North Atlantic. Over the next few centuries, anthropogenic CO_2 is then redistributed by ocean circulation and stored mostly in the upper layers of the subtropical gyres. Because of the combined effects of (i) weakening buffering capacity, (ii) warming-induced lower solubility, (iii) changes in wind stress and (iv) changes in ocean circulation, there is a high confidence that the ocean sink will weaken in the future. Here, we use IPCC-class Earth System Model (ESM) simulations following the SSP1-2.6 and SSP5-8.5 climate change scenarios extended to the year 2300 to reveal that anthropogenic CO_2 begins to outgas in the subtropical gyres of both hemispheres during the summer months of the 21st century. In 2100, about 53% of the surface ocean experience outgassing at least one month in a year in SSP1-2.6, against 37% in SSP5-8.5. After 2100, this fraction keeps increasing, reaching 63% by 2300 in SSP5-8.5 while stabilizing at 55% in SSP1-2.6. This outgassing pattern is driven by the rapid increase in oceanic pCO_2, faster than the atmospheric pCO_2, due to the combined effect of both rapid warming and long-term accumulation of anthropogenic carbon in these regions. These findings call for increased observation efforts in these areas, particularly in the subtropical gyres of the Southern Hemisphere, in order to detect future release of anthropogenic carbon and accurately constrain the future carbon budget.

1. Introduction

The ocean responds to the anthropogenic perturbation by uptaking roughly 25% of the human induced carbon emissions annually (Friedlingstein *et al* 2022), altering in the meantime its physical and biogeochemical state. Under a steady increase in atmospheric CO_2, the ocean acts as a negative feedback by absorbing the excess heat and CO_2 from the atmosphere (Friedlingstein *et al* 2006, Roy *et al* 2011). Nevertheless, the feedback has been shown to be non-linear over long-term stabilizing or overshoot scenarios (Schwinger and Tjiputra 2018, Asaadi *et al* 2023). Therefore, accurately predicting the future evolution of climate requires a better understanding of the ocean's long-term response and capacity to mitigate or reinforce human-induced climate change.

Presently, the CO_2 emitted by human activities enters the ocean interior through ventilation regions and is redistributed and stored predominantly in the North Atlantic, the subtropical gyres and the Southern Ocean (Sabine *et al* 2004, Gruber *et al* 2009, 2019a, Sabine and Tanhua 2010, Khatiwala *et al* 2013). Since anthropogenic carbon (C^{ant}) in the ocean cannot be directly observed, models have been adopted to determine its long-term air-sea fluxes and transport pathways variability (Wetzel *et al* 2005, Gorgues *et al* 2010, Tjiputra *et al* 2010). Ocean inversion methods, combining observational data with dynamical models, have also been applied to estimate of the C^{ant} flux (Gloor *et al* 2003, Mikaloff Fletcher *et al* 2006, Gruber *et al* 2009, DeVries 2014). The Southern Ocean is one of the main gateways for C^{ant}, representing about 40% of the contemporary oceanic

C^{ant} uptake (DeVries 2014). C^{ant} is then redistributed in the interior by the ocean mixing and circulation. The net lateral transport of C^{ant} is mostly northward, (Gruber *et al* 2009, DeVries 2014, Bourgeois *et al* 2022). However, this vertically integrated view obstructs the more complex patterns (Nakano *et al* 2015). C^{ant} is subducted out of the mixed layer mostly in the mid and high-latitude (between 20° and 60° latitudes in both hemispheres, Bopp *et al* 2015, Davila *et al* 2022). Below the mixed layer, C^{ant} is transported following the mean large scale overturning circulation (Gruber *et al* 2009, Nakano *et al* 2015). It is transported equatorward in the intermediate water layers, by the subtropical or Subantarctic Mode Waters or the Antarctic Intermediate Water. In the deeper layers, it is transported northward in the Pacific, while it is transported southward in the Atlantic.

The anthropogenic CO_2 also re-emerges from the deep ocean, notably through the subtropical or shallow overturning circulation (Nakano *et al* 2015, Iudicone *et al* 2016). The upwelling at the equator transports carbon across the base of the mixed layer (Bopp *et al* 2015, Zhai *et al* 2017). Moreover, the subduction (downward flux) in the rest of the ocean results from a compensation between strong upward and downward fluxes (Toyama *et al* 2017). Such re-emergence can strongly inhibit the ability of the ocean to further uptake C^{ant} (Rodgers *et al* 2020). On top of that, due to the combined effects of (i) the slowing down of the CO_2 emissions rate, (ii) weakening of the buffering capacity (Jiang *et al* 2019, 2023, Arora *et al* 2020), (iii) decrease in warming-induced solubility (Tjiputra *et al* 2010, Katavouta and Williams 2021), (iv) changes in wind stress (Bronselaer *et al* 2016, 2018) and ocean circulation (Tjiputra *et al* 2010, Gruber *et al* 2019a, Arora *et al* 2020, Bronselaer and Zanna 2020, Katavouta and Williams 2021), there is a high confidence that the ocean sink will weaken in the future even if the extent of the weakening is scenario-dependent Arora *et al* 2020, IPCC 2021). Considering the decline in oceanic carbon sink and the re-emergence of the C^{ant} into the surface ocean, our study addresses the question of when and where the previously absorbed C^{ant} by the ocean will be released back into the atmosphere, and whether these outgassing signals will be strong enough to emerge from the background inter-annual variability and be detectable.

The concept of time of emergence or departure has been used extensively in recent works to assess the emergence of anthropogenically induced signals such as warming, acidification, air-sea CO_2 flux trends, and primary production decline (Henson *et al* 2010, Mora *et al* 2013, Keller *et al* 2014, Rodgers *et al* 2015, Bertini and Tjiputra 2022, Tjiputra *et al* 2023). Time of emergence is defined as the time when the considered signal of a variable exceeds its respective background noise. The background noise is commonly

defined as twice the standard deviation of either an ensemble of simulations (McKinley *et al* 2016, Schlunegger *et al* 2019) or time series from preindustrial simulations (Henson *et al* 2010, 2017, Christian 2014, Keller *et al* 2014, Tjiputra *et al* 2023), representing internal or inter-annual climate variability. Statistically, using twice the standard deviation ensures that the signal exceed 95% of the values in the background noise. Some alternative choices for the noise can be one standard deviation (confidence interval of 67%, Rodgers *et al* 2015) or minimum and maximum values (Mora *et al* 2013). The time of emergence is a useful concept for getting information about the detectability of a signal as well as the pace of climate change impacts.

The main goal of this work is to identify the time of emergence of C^{ant} outgassing and its drivers in the different ocean regions. The next section describes the model and global warming scenarios used, the definition of the time of emergence used for C^{ant} outgassing as well as the diagnostic applied to identify the drivers of the emergence. Following the method section, the results are presented and discussed.

2. Methods

2.1. Model configurations

We use the second version of the Norwegian Earth System Model (NorESM2-LM, Seland *et al* 2020a, 2020b) built with atmospheric, ocean, sea-ice, and land modules. The ocean component of NorESM2-LM is the Bergen Layered Ocean Model (BLOM) coupled with the isopycnic coordinate Hamburg Ocean Carbon Cycle (iHAMOCC) model for ocean biogeochemistry (Tjiputra *et al* 2020). iHAMOCC represents the lower trophic biological productivity in the upper ocean by including one phytoplankton, one zooplankton compartment, multiple limiting nutrients (nitrate, phosphate, and dissolved iron), dissolved organic carbon and particulate matters. A fixed stoichiometry redfield ratio is used to govern the fluxes of nutrients and carbon among the different ecosystem compartments.

The inorganic carbon chemistry in iHAMOCC is based on the Ocean Carbon cycle Model Intercomparison Project protocols. It computes the partial pressure of CO_2 gas in the surface layer (pCO_2) based on the temperature, salinity, dissolved inorganic carbon (DIC) and alkalinity concentrations. The air-sea CO_2 fluxes is computed according to Wanninkhof (2014) taking into account surface wind speed, Schmidt number, gas solubility, atmospheric pCO_2, and surface ocean pCO_2. In order to explicitly estimate the C^{ant} fluxes and inventory in the ocean, NorESM2-LM simulates a set of 'natural' carbon tracers (include DIC, alkalinity, and $CaCO_3$) that are constrained by a fixed preindustrial control atmospheric CO_2 concentration of 284.7 ppm

during the air-sea gas exchange. Thus, C^{ant} is calculated as the difference between the total and natural DIC tracers (Tjiputra *et al* 2020). It should be mentioned that NorESM2-LM does not consider natural carbon tracers in the sediment, as we assume that the long timescale of sediment dynamic does not play a major role in our relatively short transient timescale. Indeed, C^{ant} interaction with the sediment occur at multi-millennial time scales (Archer *et al* 1997), which is considerably longer than the periods (1850–2300) analyzed here. Finally, it is noteworthy that even though our methodological choice can provide an estimates of the partition between anthropogenic and natural carbon, other approaches also exist, e.g. using labeled carbon tracer (Holzer and DeVries 2022), which could give different results.

2.2. Scenarios and simulations

Three model experiments were performed following the CMIP6 framework and as described in O'Neill *et al* (2016): the historical (1850–2014) and the SSP1-2.6 and SSP5-8.5 extended future scenarios (2015–2300). All the simulations are forced with prescribed atmospheric greenhouse gas concentrations, aerosol emissions and land-use change forcings (Hurtt *et al* 2020, Ma *et al* 2020, Meinshausen *et al* 2020). In such concentration-forced simulations, the ocean and land carbon cycle react to atmospheric CO_2 concentrations, which are prescribed via global mean time series, but do not feed back on the atmospheric CO_2. The historical scenario follows forcings largely based on available observations. The SSP1-2.6 scenario is on the low end of the radiative forcing. After a brief increase at the beginning of the 21st century, the CO_2 emissions decrease and atmospheric CO_2 concentrations stabilize. The SSP5-8.5 is on the high end of the radiative forcing with the carbon emissions increasing until 2080 after which they start to slowly decline to reach zero in 2250. The simulations outputs are available online (Tjiputra *et al* 2023).

Following the rising atmospheric CO_2, the global surface air temperature increases, reaching $+1.3\,°C$ with no overshoot in SSP1-2.6 and $+3.94\,°C$ in SSP5-8.5 by 2100, relative to the preindustrial level (Seland *et al* 2020a). Beyond 2100, temperature stays stable in SSP1-2.6 while it keeps increasing in SSP5-8.5 reaching about $+10.7\,°C$ by 2300. Compared to other ESMs, NorESM2-LM has a low climate sensitivity to atmospheric CO_2 accumulation: TCRE of 1.32 $°C\,EgC^{-1}$ versus 1.32–2.30 $°C\,EgC^{-1}$ for 10 other ESMs (Arora *et al* 2020). The warming in NorESM2-LM is on the low end of the projected range from other models (IPCC 2021). By 2100, others ESMs project $+1.3\,°C$ to $+2.8\,°C$ of warming in SSP1-2.6 and $+3.6\,°C$ to $+6.5\,°C$ in SSP5-8.5. Beyond 2100, only few ESMs have performed global warming scenarios. They project a continuous warming reaching $+11\,°C$ to $+17.5\,°C$ in SSP5-8.5 while temperature stabilizes between $+1\,°C$ to $+2.5\,°C$ in SSP1-2.6 (IPCC 2021, Koven *et al* 2022).

In addition, to isolate the effect of atmospheric CO_2 increase from the impact of global warming, we also used the so-called biogeochemical coupled (BGC) simulation (as opposed to the fully coupled simulations described before). In this simulation, the atmospheric CO_2 follows that of SSP5-8.5, but the CO_2 added to the atmosphere is not radiatively active, and does not cause global warming.

2.3. Carbon fluxes in the different scenarios

Globally, the total carbon uptake simulated by NorESM2-LM increases during the historical period (black line in figure 1(a)) and captures well the observed long-term trend, though slightly overestimated. In both global warming scenarios, the uptake keeps increasing, reaching a maximum rate then decreases. In SSP5-8.5 (figure 1(a), red line), the maximum global uptake occurs around 2080 then steadily decreases until the end of the simulation period. In SSP1-2.6 (figure 1(a), blue line), the maximum is reached around 2030 and the global uptake is very close to zero from 2100 onward. The long term evolution of ocean carbon uptake along the simulations is mostly due to the uptake of C^{ant} (figure 1(b)). The global mean natural carbon fluxes are close to zero from 1850 to 2300.

The NorESM2-LM model reproduces the spatial patterns of the C^{ant} air-sea flux as understood from the literature on the historical period (figure 1(c)). The uptake is particularly strong in the Southern Ocean, the North Atlantic and the tropics (Mikaloff Fletcher *et al* 2006, Corbière *et al* 2007, Gruber *et al* 2009, 2019b, Ridge and McKinley 2020, Brown *et al* 2021). In SSP1-2.6, in the 2090s (figure 1(d)), the close to zero global mean C^{ant} air-sea flux results from the compensation between regions of uptake and outgassing C^{ant}. The Southern Ocean outgases C^{ant} between 40 °S and 60 °S while still uptakes C^{ant} south of 60 °S. The subpolar North Atlantic and North Pacific, as well as the equatorial band, also outgas C^{ant}. In the 2290s (figure 1(e)), the spatial distributions of C^{ant} fluxes are similar, though attenuated. In SSP5-8.5, in the 2090s (figure 1(f)), C^{ant} uptake patterns are similar to the 1990s but stronger, with particularly strong uptake in the Southern Ocean, the North Atlantic and the tropics. In the 2290s (figure 1(g)), the global mean C^{ant} uptake results from a compensation between regions of C^{ant} uptake and outgas. As in SSP1-2.6, the strongest fluxes are simulated in the Southern Ocean: outgassing between 40 °S and 60 °S and uptaking south of 60 °S. In addition, the subpolar North Atlantic and North Pacific, as well as parts of the equatorial band also outgas C^{ant}.
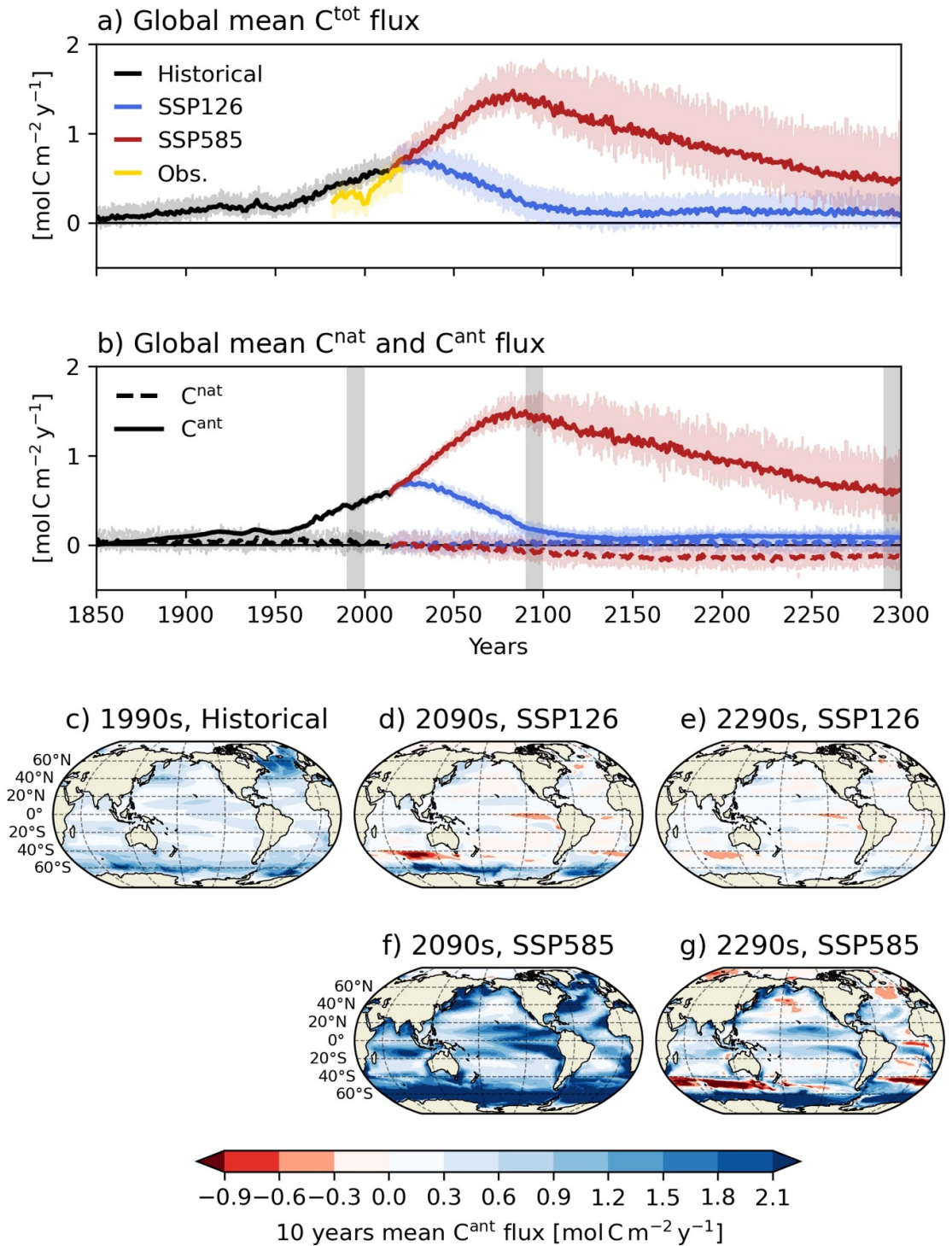
Figure 1. Air-sea carbon fluxes between 1850 and 2300, for the historical and two extended scenarios with the NorESM2-LM. (a) Time series of the total carbon flux averaged globally in the historical (black), SSP1-2.6 (blue) and SSP5-8.5 (red) simulations. The yellow line shows the observed carbon flux from Landschützer *et al* (2020). The thick lines show the yearly average, while the shadings show the monthly average. (b) Same as (a) but separating the natural (dashed line) from the anthropogenic (plain line) carbon fluxes. Maps of the C^{ant} flux average on (c) 1990–1999, (d), (f) 2090–2099 and (e), (g) 2290–2299 for the historical, SSP1-2.6 and SSP5-8.5 simulations. Vertical grey shading in (b) shows the 3 different time periods depicted in panels (c)–(g). Positive values stand for ocean carbon uptake.

2.4. Time of anthropogenic carbon outgassing

The main goal of this work is to determine when and where C^{ant} is released back into the atmosphere, i.e $F_{co_2}^{tot}(t,i) - F_{co_2}^{nat}(t,i) \leqslant 0$ where $F^{xxx}(t,i)$ is the total or the natural air-sea carbon flux for time t and

location i. We analyze monthly average rather than annual average because there is a strong seasonality in the C^{ant} flux (figure 2). For instance, net annual C^{ant} uptakes are simulated in some regions even though they release C^{ant} during summer, because of
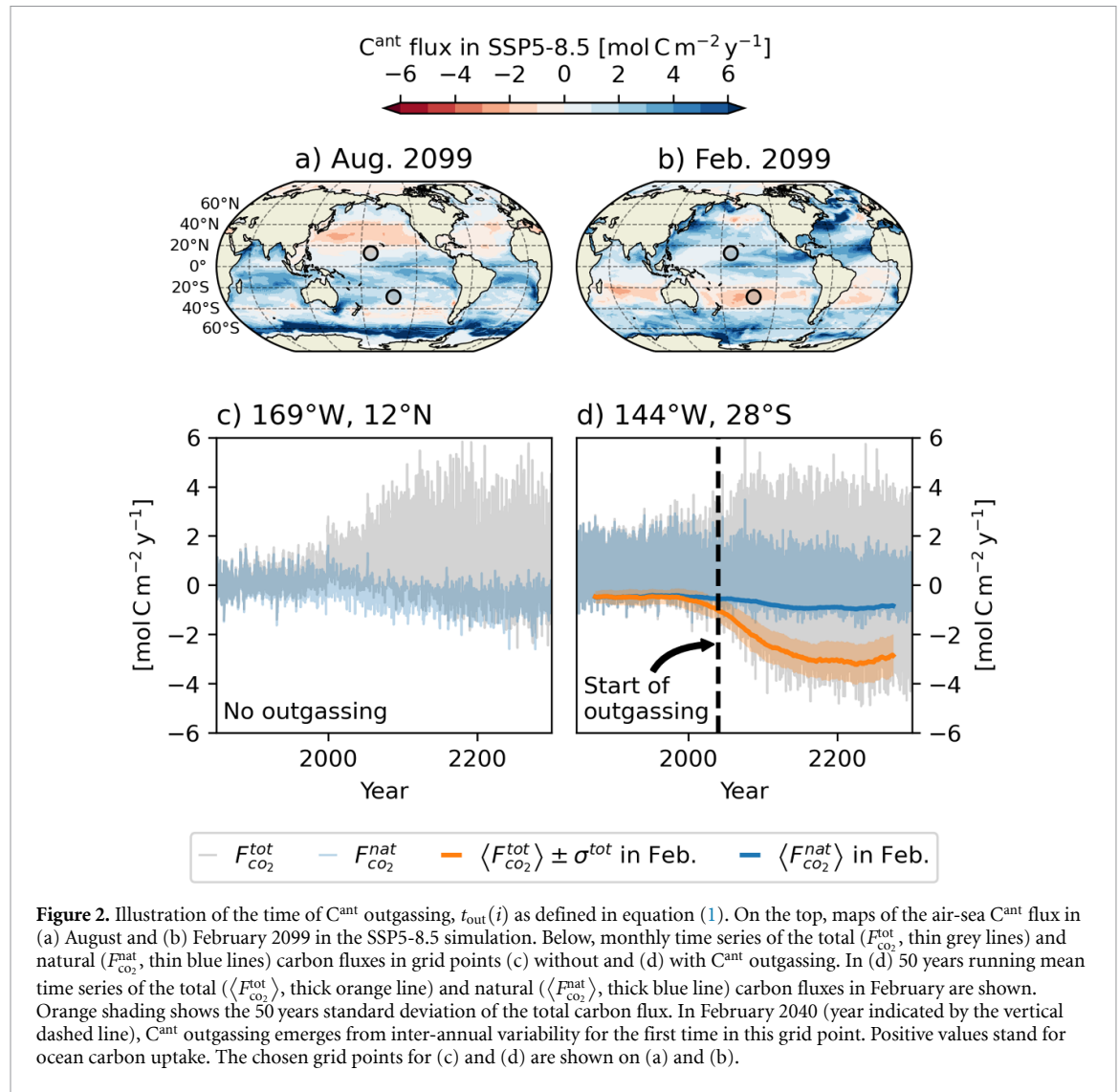
Figure 2. Illustration of the time of C^{ant} outgassing, $t_{out}(i)$ as defined in equation (1). On the top, maps of the air-sea C^{ant} flux in (a) August and (b) February 2099 in the SSP5-8.5 simulation. Below, monthly time series of the total ($F^{tot}_{co_2}$, thin grey lines) and natural ($F^{nat}_{co_2}$, thin blue lines) carbon fluxes in grid points (c) without and (d) with C^{ant} outgassing. In (d) 50 years running mean time series of the total ($\langle F^{tot}_{co_2} \rangle$, thick orange line) and natural ($\langle F^{nat}_{co_2} \rangle$, thick blue line) carbon fluxes in February are shown. Orange shading shows the 50 years standard deviation of the total carbon flux. In February 2040 (year indicated by the vertical dashed line), C^{ant} outgassing emerges from inter-annual variability for the first time in this grid point. Positive values stand for ocean carbon uptake. The chosen grid points for (c) and (d) are shown on (a) and (b).

the stronger uptake in winter. Moreover, for detecting when the C^{ant} outgassing will emerge from the background inter-annual variability, we use a 50 years running mean of the carbon fluxes ($\langle F^{tot}_{co_2} \rangle (t,i)$ and $\langle F^{nat}_{co_2} \rangle (t,i)$) as well as a 50 years running standard deviation of the total carbon flux, $\sigma^{tot}(t,i)$. Thus, for any location i, we search for the time $t_{out}(i)$ (month and year) such as:

$$t_{out}(i) = \min \left\{ t : \langle F^{tot}_{co_2} \rangle (t,i) - \langle F^{nat}_{co_2} \rangle (t,i) \right.$$
$$\left. \leqslant -\sigma^{tot}(t,i) \right\}. \tag{1}$$

The time of C^{ant} outgassing defined above depends on the time window used to calculate the mean and on the threshold used for the emergence (here the standard deviation). Additional analysis show that the outgassing spatial patterns are only weakly sensitive to the time window and threshold., i.e. the regions with the earliest C^{ant} outgassing stay the same (e.g. figure S1). However, it may change

the absolute year of outgassing but not the month of outgassing.

2.5. Attribution of the anthropogenic carbon outgassing

The year of C^{ant} outgassing emergence defined in equation (1) depends on the difference between $\langle F^{tot}_{co_2} \rangle$ and $\langle F^{nat}_{co_2} \rangle$ and σ^{tot}. Since, (1) the emergence patterns are weakly sensitive to σ^{tot} (figure S1), (2) $\langle F^{nat}_{co_2} \rangle$ does not vary much along the simulations (figures 2(c) and (d)), (3) the emergence patterns are similar when using the preindustrial flux instead of $\langle F^{nat}_{co_2} \rangle$ (figure S2), then the outgassing emergence patterns are essentially determined by $\langle F^{tot}_{co_2} \rangle$. In areas where outgassing emerge earlier (see the result section), wind speed and solubility are weaker and even decrease along the 21st century (figure S3). Thus they do not strengthen the C^{ant} flux and cause earlier emergence. Therefore C^{ant} outgassing is primarily driven by evolution of the oceanic and atmospheric pCO_2.

In response to the increase in atmospheric pCO_2, the ocean takes up CO_2, thereby changing its pCO_2. In the long-term, the oceanic pCO_2 follows closely the atmospheric counterpart (Fay and McKinley 2013, Tjiputra *et al* 2014). For the ocean to release carbon, its partial pressure has to be larger than the atmospheric one. We infer that the regions where carbon outgassing emerges are also the ones where the oceanic pCO_2 increase faster than the atmospheric pCO_2. Changes in oceanic pCO_2 in turns depend on changes in the DIC content but also on the temperature, the salinity (or freshwater inputs) and the alkalinity. Following a first order Taylor expansion (Takahashi *et al* 1993, Lovenduski *et al* 2007, Goris *et al* 2015, Gallego *et al* 2018, 2020), the oceanic pCO_2 trend ($dpCO_2/dt$) can be recosntructed from the sum of three components: (i) the carbon system trend gathering the trends in DIC and alkalinity, (ii) the thermal trend and (iii) the freshwater/salinity trend (accounting for the dilution/concentration impact of freshwater on DIC and alkalinity) following equation (2).

$$\frac{dpCO_2}{dt} \simeq \frac{\overline{pCO_2} \times \overline{S}}{\gamma_C \times S_0} \times \frac{\partial C_s}{\partial t} + \frac{\overline{pCO_2} \times \overline{S}}{\gamma_A \times S_0} \times \frac{\partial A_s}{\partial t} \qquad \textbf{Carbon system}$$

$$+ \overline{pCO_2} \times \gamma_T \times \frac{\partial T}{\partial t} \qquad \textbf{Thermal}$$

$$+ \left(\frac{\overline{pCO_2} \times \overline{C_s}}{\gamma_C \times S_0} + \frac{\overline{pCO_2} \times \overline{A_s}}{\gamma_A \times S_0} + \frac{\overline{pCO_2} \times \gamma_S}{\overline{S}} \right) \times \frac{\partial S}{\partial t} \qquad \textbf{Freshwater and salinity}. \qquad (2)$$

In this equation, T and S are the sea surface temperature and salinity. C_s and A_s are the salinity-normalized DIC and alkalinity concentrations: $X_s = S_0/S \times X$. S_0 is the temporal average of S over the entire simulation. γ_X are related to the sensitivity of pCO_2 to DIC, alkalinity, salinity and temperature ($\partial pCO_2/\partial X = \overline{pCO_2}/\gamma_X$). The overbar, $\overline{X}$, stands for seasonal average of X calculated over the 50 year window. The trends, $\partial X/\partial t$, are computed as the difference in X between two consecutive 50 years period. γ_C and γ_A are computed with the pyCO2SYS module (Humphreys *et al* 2022) using the 50 years mean of DIC, alkalinity, salinity and temperature. γ_T is $0.0423\,°C^{-1}$ and γ_S is 1 (Takahashi *et al* 1993, Sarmiento and Gruber 2006).
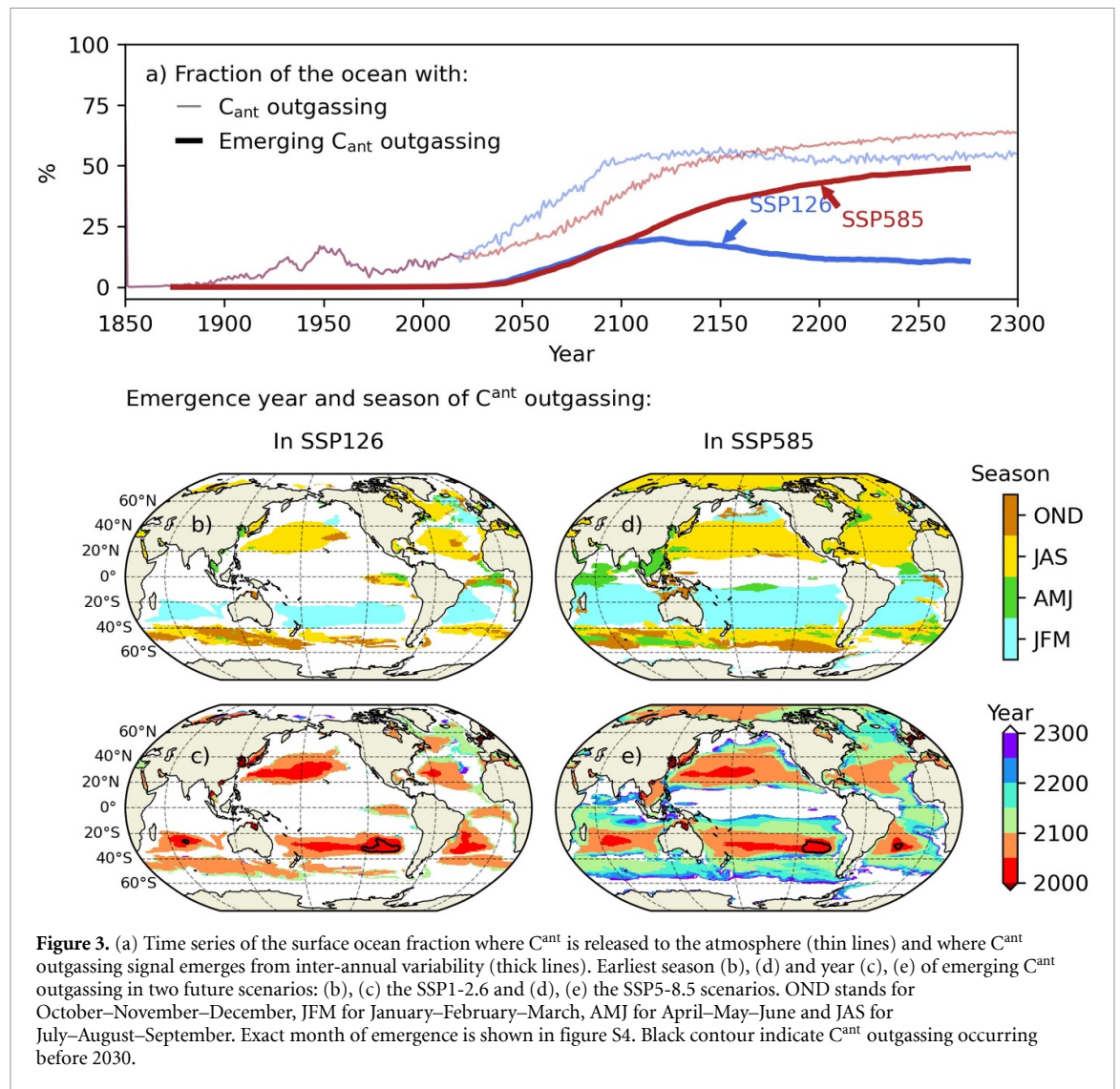
3. Results

3.1. Outgassing of anthropogenic carbon

Throughout the historical and the future warming scenarios, the simulations show that the ocean releases C^{ant} at an increasing rate. During the historical period, between 5% and 20% of the ocean area is releasing C^{ant} for at least one month annually (figure 3(a), thin lines). Nevertheless, these fluxes are too weak to emerge from their background inter-annual variability signals. Only by 2040 does outgassing signal become stronger than the inter-annual variability (figure 3(a), thick lines). The SSP1-2.6 simulation shows a larger proportion of the ocean outgassing C^{ant} than SSP5-8.5 in the 21st century. By 2100, about 53% of the surface ocean release C^{ant} for at least one month in a year in SSP1-2.6 versus only about 37% in SSP5-8.5. Nonetheless, the outgassing emerges only in 19% of the ocean in both simulations by the end of the 21st century. After 2100, the fraction of the ocean outgassing C^{ant} continues to increase in SSP5-8.5, reaching 63% by 2300, while it stabilizes at around 55% in SSP1-2.6. The ocean fraction where outgassing emerge from inter-annual variability keeps increasing in SSP5-8.5, reaching 49% by 2300, while it decreases in SSP1-2.6, stabilizing at 12%.

The spatial pattern of the season when C^{ant} outgassing emerges coincides essentially with well-known oceanic regions (figures 3(b) and (d)). The subtropical gyres outgas C^{ant} in summer: JAS for the Northern Hemisphere and JFM for the Southern Hemisphere (see also figure S4 for exact month) . These patterns are very similar in both scenarios. In the Southern Ocean (40–60 °S), the majority of C^{ant} outgassing occurs in winter (JAS), although there are some regional differences (such as in spring or fall), but remain relatively consistent across both scenarios. In the eastern part of the the North Atlantic (40 °N–60 °N), Cant outgassing emergence occurs in summer (JAS) in SSP5-8.5, while it occurs mostly in winter (JFM) in SSP1-2.6. In the Arctic ($<70°N$), C^{ant} outgassing emergence occurs only in SSP5-8.5 in summer.

The spatial pattern of the year when C^{ant} outgassing emerges from inter-annual variability also coincides with distinct oceanic regions (figures 3(c) and (e)). The earliest emergence occurs in the subtropical gyres in both scenarios. In some regions, C^{ant} outgassing starts before 2030 (as shown by the black contour in figures 3(c) and (e)). The farther away from the centre of the gyre, the later the outgassing emerges. In SSP1-2.6, most of the C^{ant} outgassing emerge before 2100. After 2100, outgassing emergence starts to become detectable in parts of the North Atlantic. In SSP5-8.5, C^{ant} emergence continues to

Figure 3. (a) Time series of the surface ocean fraction where C^{ant} is released to the atmosphere (thin lines) and where C^{ant} outgassing signal emerges from inter-annual variability (thick lines). Earliest season (b), (d) and year (c), (e) of emerging C^{ant} outgassing in two future scenarios: (b), (c) the SSP1-2.6 and (d), (e) the SSP5-8.5 scenarios. OND stands for October–November–December, JFM for January–February–March, AMJ for April–May–June and JAS for July–August–September. Exact month of emergence is shown in figure S4. Black contour indicate C^{ant} outgassing occurring before 2030.

occur throughout the simulation (as expected from figure 3(a)). The model simulates no detectable C^{ant} outgassing in the southernmost part of the Southern Ocean or in most of the equatorial band.
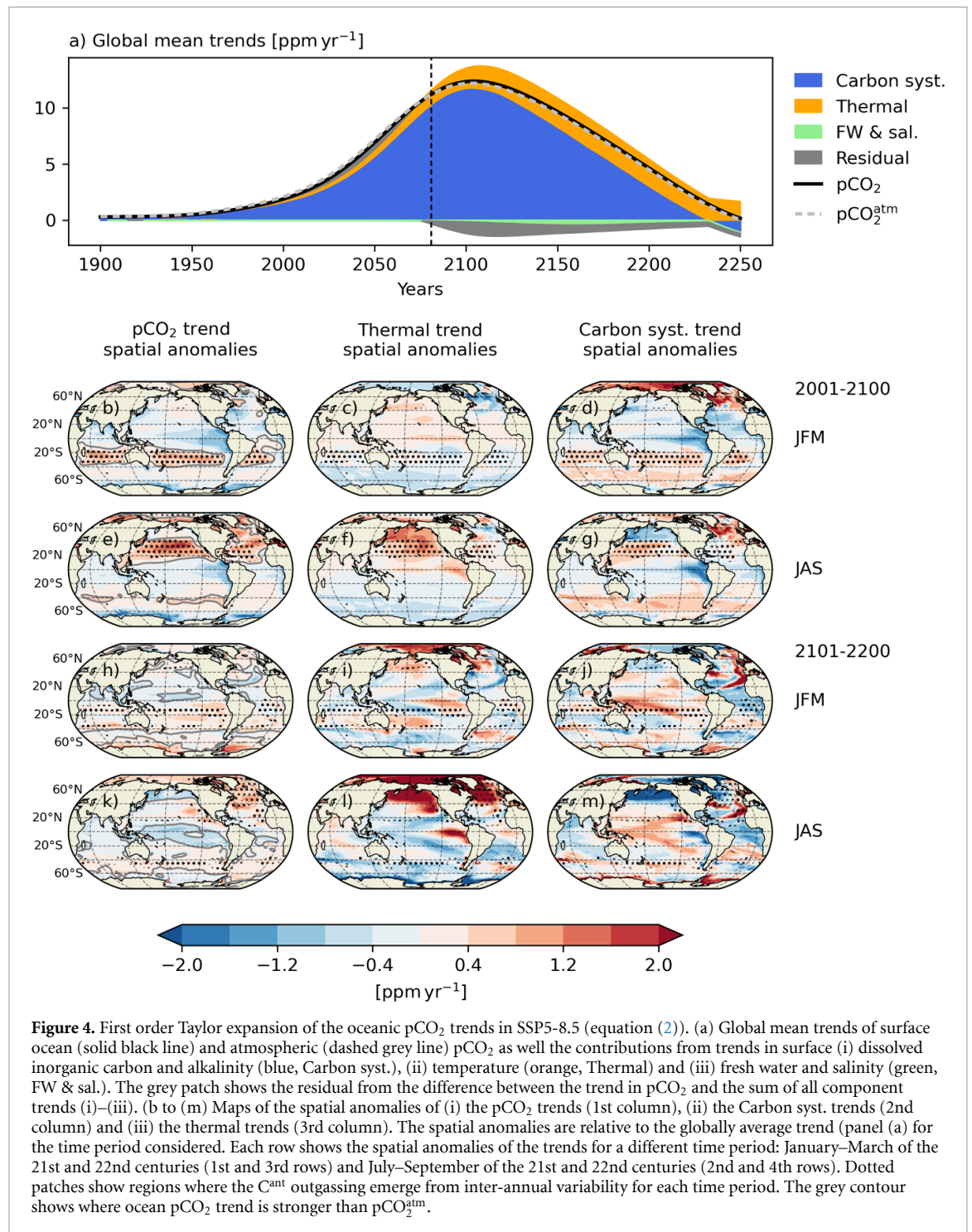
3.2. Drivers of the carbon outgassing in SSP5-8.5

Here, applying equation (2), we seek to unravel the drivers of the C^{ant} outgassing. In particular, we aim to explain why the outgassing signal emerges earlier in the subtropical gyres than in the higher latitude or at the equator. Since the patterns of outgassing emergence are relatively similar between the SSP1-2.6 and SSP5-8.5, suggesting similar processes are at play, we focus our analysis on the SSP5-8.5 scenario, which has the strongest signal.

The season of the C^{ant} outgassing emergence is controlled by the drivers of pCO_2 seasonality (see figure S5 and Sarmiento and Gruber 2006, Landschützer *et al* 2018). C^{ant} outgassing signal emerges when pCO_2 is maximum. In the mid-latitudes (15–40 °N/S), pCO_2 reaches its highest level in summer when the temperature is maximum. In the Southern Ocean (40–60 °S), the highest pCO_2

occurs in winter as a result of non-thermal processes. With the deepening of the mixed layer, water rich in natural carbon but poor in C^{ant} are entrained to the surface, leading to an increase in natural carbon but a decrease in C^{ant} at the surface. However, the total carbon content is higher than in summer and higher than it would be without C^{ant}. In addition, because of the higher carbon content (and Revelle Factor), pCO_2 is more sensitive to the increase in DIC. Altogether, it leads to the stronger outgassing of carbon (in our approach, this excess outgassing is considered as C^{ant}). In the North Atlantic, >40 °N, and in the Arctic, the outgassing signals emerge in the summer (in SSP5-8.5) when pCO_2 is maximum because of temperature and when the sea-ice extent is minimum (Notz and Community 2020).
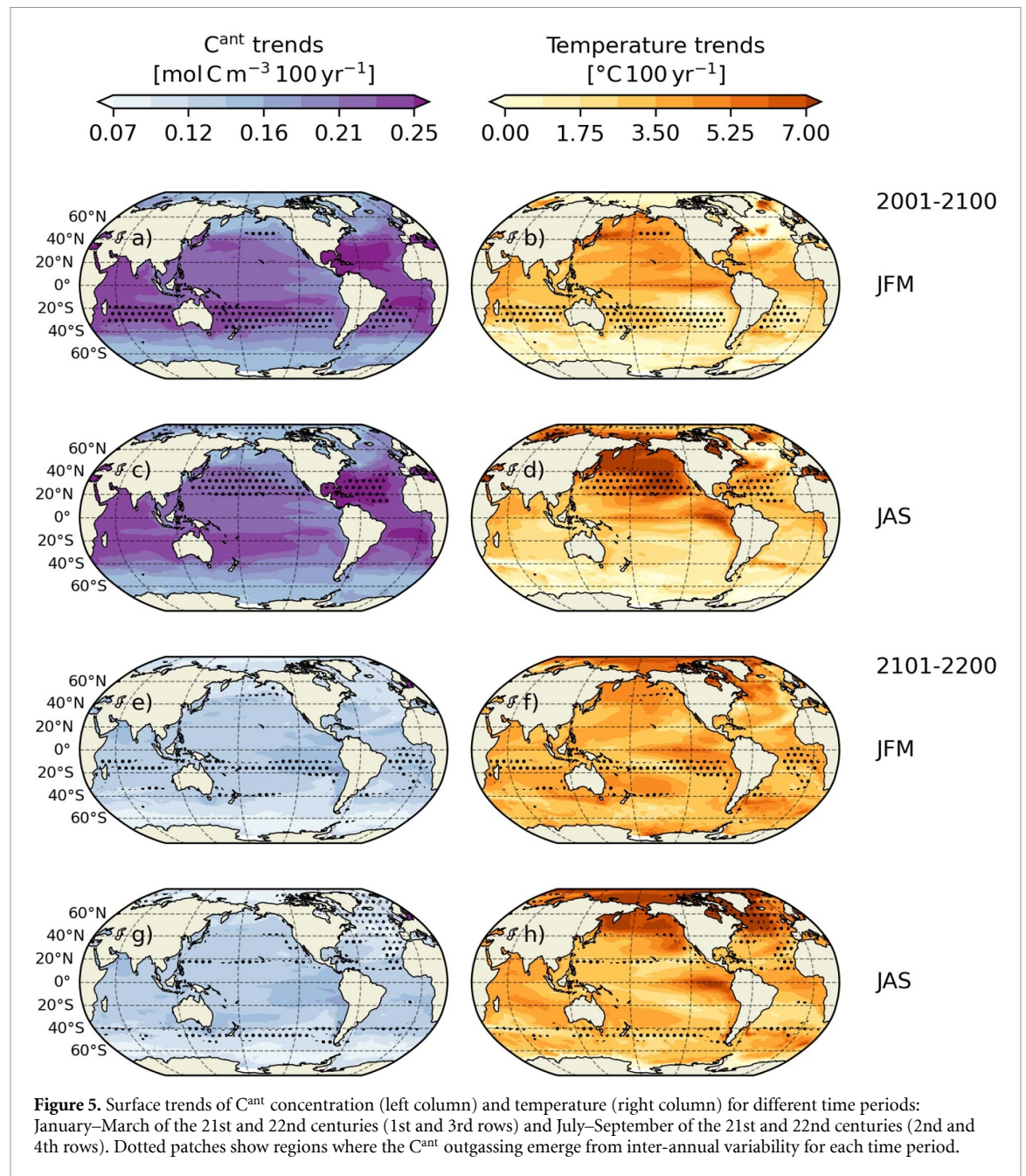
For the global average, the rate of change of oceanic pCO_2 closely follows the time evolution of atmospheric pCO_2 rate of change (solid and dashed lines in figure 4(a)), primarily driven by the ocean carbon uptake that increases the DIC content (blue patch in figure 4(a); carbon system term in equation (2)). Until 2080, the pCO_2 growth rate is higher in the

Figure 4. First order Taylor expansion of the oceanic pCO_2 trends in SSP5-8.5 (equation (2)). (a) Global mean trends of surface ocean (solid black line) and atmospheric (dashed grey line) pCO_2 as well the contributions from trends in surface (i) dissolved inorganic carbon and alkalinity (blue, Carbon syst.), (ii) temperature (orange, Thermal) and (iii) fresh water and salinity (green, FW & sal.). The grey patch shows the residual from the difference between the trend in pCO_2 and the sum of all component trends (i)–(iii). (b to m) Maps of the spatial anomalies of (i) the pCO_2 trends (1st column), (ii) the Carbon syst. trends (2nd column) and (iii) the thermal trends (3rd column). The spatial anomalies are relative to the globally average trend (panel (a) for the time period considered. Each row shows the spatial anomalies of the trends for a different time period: January–March of the 21st and 22nd centuries (1st and 3rd rows) and July–September of the 21st and 22nd centuries (2nd and 4th rows). Dotted patches show regions where the C^{ant} outgassing emerge from inter-annual variability for each time period. The grey contour shows where ocean pCO_2 trend is stronger than pCO_2^{atm}.

atmosphere than in the ocean. From 2080 onward, pCO_2 growth rate is higher in the ocean than in the atmosphere, reducing the difference and thus the carbon uptake (figure 1(a)). During the 22nd and 23rd centuries, the reductions in atmospheric growth rate and oceanic carbon uptake lead to a slow-down in oceanic pCO_2 increase. At the same time, the ocean keeps warming, and thus the thermal contribution becomes growingly more important (figure 4(a), orange patch). The freshwater input and salinity term only plays a marginal role (figure 4(a), green patch). We note that the sum of the carbon

system trend, thermal trend and freshwater and salinity trend (right-hand side in equation (2)) does not exactly match the trend in oceanic pCO_2 (left-hand side in equation (2)). However, the residual is small (figure 4(a), grey patch). From now we focus on the spatial anomalies of the trends (figures 4(b)–(m)) to identify regions where the trends are steeper/shallower than their global average. The absolute values of the trends are shown in figure S6.

As inferred above, C^{ant} outgassing emerge earlier in regions where the increase in oceanic pCO_2 is faster than its atmospheric counterpart (grey contours in

Figure 5. Surface trends of C^{ant} concentration (left column) and temperature (right column) for different time periods: January–March of the 21st and 22nd centuries (1st and 3rd rows) and July–September of the 21st and 22nd centuries (2nd and 4th rows). Dotted patches show regions where the C^{ant} outgassing emerge from inter-annual variability for each time period.

figures 4(b) and (e)). In this areas the increase in pCO_2 is also faster than the global average. For the 21st century, the faster increase in oceanic pCO_2 occurs in the subtropical gyres where outgassing signals emerge before 2100 (figures 4(b) and (e)) and this expands at the edges of the subtropical gyres during the 22nd century (figures 4(h) and (k)).

In the subtropical gyre of both hemispheres (20–40 °N/S), the fast increase in oceanic pCO_2 is driven by the accumulation of C^{ant} at the ocean surface with a significant contribution from warming in the Northern Hemisphere (figures 4 and 5). This is particularly evident during the 21st century. In the Southern Hemisphere, the fast C^{ant} accumulation (figure 5(a)) combine with rather high values of mean oceanic pCO_2 (figure S7) lead to a faster

increase of the carbon system-driven oceanic pCO_2 (figure 4(d)) while warming plays a secondary role (figures 4(c) and 5(b)). In the Northern Hemisphere, the fast C^{ant} accumulation dominates in the western part of the North Pacific while fast warming prevails in the eastern North Pacific and in the North Atlantic (figures 4(f), (g) and 5(c), (d)). In the 22nd century, the expansion of the emergence along the edges of the subtropical gyres is also driven by the fast C^{ant} accumulation (figures 4(j), (m) and 5(e) and (g)). In the subpolar gyre of the North Atlantic (40–60 °N), the rapid summer warming causes the anomalously strong pCO_2 growth (figures 4(l) and 5(h)).

The analysis of the BGC simulation (i.e. without C^{ant}-induced warming; figures S8 and S9) shows that, in the gyres core, the fast C^{ant} accumulation is still

responsible for the early outgassing even without warming. Overall, warming makes the C^{ant} outgassing to emerge earlier and in a larger portion of the ocean. In regions where warming has a major contribution in C^{ant} outgassing, the emergence signals seen in the fully coupled simulation (e.g. Arctic, North Atlantic, Equatorial Atlantic) are delayed or do not happen in the BGC simulation.

4. Discussion and conclusions

Our work shows that the accumulation of C^{ant} in the subtropical gyres of both hemispheres combined with the continuous surface warming leads to an increase in oceanic pCO_2 faster than elsewhere and faster than the atmospheric pCO_2 growth in these areas. In addition, the seasonal cycle of temperature pushes the pCO_2 toward even higher values during the summer months of the respective hemispheres. These factors lead to C^{ant} outgassing signals, which emerge beyond the inter-annual variability in most of the subtropical gyres by the end of the 21st century in two contrasting future scenarios (i.e. with and without strong climate mitigation of SSP1-2.6 and SSP5-8.5), as simulated by state-of-the-art ESM. Finally, similar results are obtained when we applied our analysis on another CMIP6 ESM, ACCESS-ESM1-5 (figures S10 and S11). This ESM is "independent" and has a climate sensitivity stronger than NorESM2-LM. Thus, despite using only one model, we consider our results to be relatively robust.

The accumulation of C^{ant} in the subtropical gyres has been previously identified in the literature with observations (Khatiwala *et al* 2013, Gruber *et al* 2019a) and models (Tjiputra *et al* 2010, Bopp *et al* 2015). This C^{ant} accumulation pattern is driven by the large-scale circulation, e.g. the convergence of Ekman transport at the surface of the subtropical gyres and the formation and equatorward transport of mode and intermediate waters at sub-surface. The convergence of subsurface C^{ant} into the subtropical gyres is also consistent with the early emergence of subsurface ocean acidification signals in these regions projected across an ensemble of CMIP6 ESMs (Tjiputra *et al* 2023). The surface warming pattern simulated in NorESM2-LM model over the 21st century is consistent with that identified in other ESMs (IPCC 2021). This future warming pattern is is also consistent with the simulated warming over the historical period in models (IPCC 2021), consistent with the observed long-term temperature change (Olonscheck *et al* 2020). Finally, Tjiputra *et al* (2014) show that ESMs simulate the strongest long-term annual trends in pCO_2 in subtropical gyres, in good agreement with observational data.

Since it is not possible to clearly identify the CO_2 molecule originating from human activities, the distinction between natural and anthropogenic air-sea CO_2 flux is often a methodological choice. In this work and as usually in the Earth system modeling world, the C^{ant} air-sea flux is the difference between the total and natural carbon fluxes. With this choice, changes in the natural CO_2 flux driven by global warming are correctly not accounted for as anthropogenic. However, with this approach, we cannot make the distinction between C^{ant} and natural carbon outgassing due to an increase in the Revelle Factor. This can notably be the case in the Southern Ocean during winter, where pCO_2 is more sensitive to the entrainment of deep water rich in natural DIC. This caveat has been explored in recent work suggesting that the invasion of C^{ant} into the ocean would lead to the release of natural carbon because of changes in carbon chemistry (Holzer and DeVries 2022). In other words, the net uptake of the C^{ant} that the model simulates in our work would actually result from an even stronger uptake of C^{ant} balanced by the release of natural carbon. Thus, the actual C^{ant} outgassing may occur later than estimated here.

In addition to the definition of C^{ant}, the time of emergence identified here is not without its uncertainties. The inter-annual variability represented in ESMs is generally underestimated compared to observation, even though the variability in observation is potentially overestimated due to the sparse spatial and temporal coverage of surface ocean pCO_2, especially in the Southern Hemisphere (Gloege *et al* 2021, Hauck *et al* 2023). These uncertainties are likely to modify the year of emergence, even if the spatial patterns should remain the same (figure S1). Our model simulations are configured as CO_2 concentration driven and not emission driven. Thus, the fluxes of carbon by the ocean does not feed back to the atmospheric concentration, which may affect the determination of C^{ant} outgassing timescale. Finally, though a useful indication, the time of emergence usually defines a lower bound for the detection horizon of a signal (Schlunegger *et al* 2019) because measurement uncertainty is not included.

Our findings show that key regions of future C^{ant} outgassing are the subtropical gyres in the summer months and the Southern Ocean in the winter months, implying that a long-term monitoring system in these domains would be highly valuable. Our analysis focuses on the monthly timescale, allowing us to consider different mechanisms acting at seasonal time scales (e.g. stronger thermal effect during summer). Indeed, previous works looking at the emergence of the trends in annual ocean CO_2 uptake give opposite results, with the subtropics having the latest time of emergence (McKinley *et al* 2016, Schlunegger *et al* 2019). This late emergence is due to the weak annual trends resulting from the opposing trends toward outgassing in summer and uptake in winter (Schlunegger *et al* 2019). This is a consequence of the strong seasonality in pCO_2, which is further enhanced in the future climate scenarios (Gallego *et al* 2018, Landschützer *et al* 2018). Though

surface pCO_2 in the Northern Hemisphere subtropical gyres are relatively well monitored, subtropical gyres in the Southern Hemisphere are considerably under observed (Tjiputra *et al* 2014, Gloege *et al* 2022). Notably, the South Pacific subtropical gyre has vast areas without any observational data. Given that these regions will likely release anthropogenic carbon early, our work calls for largely reinforcing the observational effort in the subtropical gyres of the Southern Hemisphere.

Finally, our study underlines the importance of understanding the long-term response of previously absorbed anthropogenic carbon by the ocean in future climate change scenarios when considering the allowable future carbon emissions toward certain climate targets (e.g. the Paris Agreement). For instance, in a future scenario with net zero emissions, one should take into account the ocean reversing role from a net carbon sink to a net carbon source, as the previously absorbed carbon is released back to the atmosphere.

Data availability statement

The data that support the findings of this study are openly available at the following URL/DOI: https://doi.org/10.5281/zenodo.10027152.

Acknowledgments

ORCID iD

Damien Couespel ⬤ https://orcid.org/0000-0003-2244-1352

References

Angeles Gallego M, Timmermann A, Friedrich T and Zeebe R E 2018 Drivers of future seasonal cycle changes in oceanic pCO_2 *Biogeosciences* **15** 5315–27

Angeles Gallego M, Timmermann A, Friedrich T and Zeebe R E 2020 Anthropogenic Intensification of Surface Ocean Interannual pCO_2 Variability *Geophys. Res. Lett.* **47** e2020GL087104

Archer D, Kheshgi H and Maier-Reimer E 1997 Multiple timescales for neutralization of fossil fuel CO2 *Geophys. Res. Lett.* **24** 405–8

Arora V K *et al* 2020 Carbon–concentration and carbon–climate feedbacks in CMIP6 models and their comparison to CMIP5 models *Biogeosciences* **17** 4173–222

Asaadi A, Schwinger J, Lee H, Tjiputra J, Arora V, Séférian R, Liddicoat S, Hajima T, Santana-Falcón Y and Jones C D 2023 Carbon cycle feedbacks in an idealized and a scenario simulation of negative emissions in CMIP6 Earth system models *EGUsphere* **2023** 1–36

Bertini L and Tjiputra J 2022 Biogeochemical timescales of climate change onset and recovery in the North Atlantic interior under rapid atmospheric CO2 forcing *J. Geophys. Res.* **127** e2021JC017929

Bopp L, Lévy M, Resplandy L and Sallée J-B 2015 Pathways of anthropogenic carbon subduction in the global ocean *Geophys. Res. Lett.* **42** 6416–23

Bourgeois T, Goris N, Schwinger J and Tjiputra J F 2022 Stratification constrains future heat and carbon uptake in the Southern Ocean between 30° S and 55° S *Nat. Commun.* **13** 340

Bronselaer B and Zanna L 2020 Heat and carbon coupling reveals ocean warming due to circulation changes *Nature* **584** 227–33

Bronselaer B, Zanna L, Munday D R and Lowe J 2016 The influence of Southern Ocean winds on the North Atlantic carbon sink *Glob. Biogeochem. Cycles* **30** 844–58

Bronselaer B, Zanna L, Munday D R and Lowe J 2018 Southern Ocean carbon-wind stress feedback *Clim. Dyn.* **51** 2743–57

Brown P J *et al* 2021 Circulation-driven variability of Atlantic anthropogenic carbon transports and uptake *Nat. Geosci.* **14** 571–7

Corbière A, Metzl N, Réverdin G, Brunet C and Takahashi T 2007 Interannual and decadal variability of the oceanic carbon sink in the North Atlantic subpolar gyre *Tellus* B **59** 168–78

Davila X, Gebbie G, Brakstad A, Lauvset S K, McDonagh E L, Schwinger J and Olsen A 2022 How Is the Ocean Anthropogenic Carbon Reservoir Filled? *Glob. Biogeochem. Cycles* **36** e2021GB007055

DeVries T 2014 The oceanic anthropogenic CO2 sink: storage, air-sea fluxes and transports over the industrial era *Glob. Biogeochem. Cycles* **28** 631–47

Fay A R and McKinley G A 2013 Global trends in surface ocean pCO2 from in situ data *Glob. Biogeochem. Cycles* **27** 541–57

Friedlingstein P *et al* 2006 Climate–carbon cycle feedback analysis: results from the C4MIP Model intercomparison *J. Clim.* **19** 3337–53

Friedlingstein P *et al* 2022 Global carbon budget 2021 *Earth Syst. Sci. Data* **14** 1917–2005

Gloege L *et al* 2021 Quantifying errors in observationally based estimates of ocean carbon sink variability *Glob. Biogeochem. Cycles* **35** e2020GB006788

Gloege L, Yan M, Zheng T and McKinley G A 2022 Improved quantification of ocean carbon uptake by using machine learning to merge global models and pCO_2 data *J. Adv. Model. Earth Syst.* **14** e2021MS002620

Gloor M, Gruber N, Sarmiento J, Sabine C L, Feely R A and Rödenbeck C 2003 A first estimate of present and preindustrial air-sea CO2 flux patterns based on ocean interior carbon measurements and models *Geophys. Res. Lett.* **30** 10-1–10-4

Gorgues T, Aumont O and Rodgers K B 2010 A mechanistic account of increasing seasonal variations in the rate of ocean uptake of anthropogenic carbon *Biogeosciences* **7** 2581–9

Goris N, Tjiputra J, Schwinger J and Heinze C 2015 Responses of carbon uptake and oceanic pCO2 to climate change in the North Atlantic: a model study with the Bergen Earth System Model *Glob. Biogeochem. Cycles* **29** 1567–83

Gruber N *et al* 2009 Oceanic sources, sinks and transport of atmospheric CO2 *Glob. Biogeochem. Cycles* **23** n/a

Gruber N *et al* 2019a The oceanic sink for anthropogenic CO2 from 1994 to 2007 *Science* **363** 1193–9

Gruber N, Landschützer P and Lovenduski N S 2019b The variable Southern ocean carbon sink *Annu. Rev. Marine Sci.* **11** 159–86

Hauck J, Nissen C, Landschützer P, Rödenbeck C, Bushinsky S and Olsen A 2023 Sparse observations induce large biases in estimates of the global ocean CO2 sink: an ocean model subsampling experiment *Phil. Trans. R. Soc.* A **381** 20220063

Henson S A, Beaulieu C, Ilyina T, John J G, Long M C, Seferian R, Tjiputra J and Sarmiento J L 2017 Rapid emergence of climate change in environmental drivers of marine ecosystems *Nat. Commun.* **8** 14682

Henson S A, Sarmiento J L, Dunne J P, Laurent Bopp I D L, Doney S C, John J and Beaulieu C 2010 Detection of anthropogenic climate change in satellite records of ocean chlorophyll and productivity *Biogeosciences* **7** 621–40

Holzer M and DeVries T 2022 Source-labeled anthropogenic carbon reveals a large shift of preindustrial carbon from the ocean to the atmosphere *Glob. Biogeochem. Cycles* **36** e2022GB007405

Humphreys M P, Lewis E R, Sharp J D and Pierrot D 2022 PyCO2SYS v1.8: Marine carbonate system calculations in Python *Geosci. Model Dev.* **15** 15–43

Hurtt G C *et al* 2020 Harmonization of global land use change and management for the period 850–2100 (LUH2) for CMIP6 *Geosci. Model Dev.* **13** 5425–64

IPCC 2021 Climate Change 2021: The physical science basis *Contribution of Working Group I to the Sixth Assessment Report of the Intergovernmental Panel on Climate Change* ed V Masson-Delmotte *et al* (Cambridge University Press) (https://doi.org/10.1017/9781009157896)

Iudicone D, Rodgers K B, Plancherel Y, Aumont O, Ito T, Key R M, Madec G and Ishii M 2016 The formation of the ocean's anthropogenic carbon reservoir *Sci. Rep.* **6** 35473

James R C 2014 Timing of the departure of ocean biogeochemical cycles from the preindustrial state *PLoS One* **9** e109820

Tjiputra J F *et al* 2020 Ocean biogeochemistry in the Norwegian Earth System Model version 2 (NorESM2) *Geosci. Model Dev.* **13** 2393–431

Jiang Li-Q *et al* 2023 Global surface ocean acidification indicators from 1750 to 2100 *J. Adv. Model. Earth Syst.* **15** e2022MS003563

Jiang Li-Q, Carter B R, Feely R A, Lauvset S K and Olsen A 2019 Surface ocean pH and buffer capacity: past, present and future *Sci. Rep.* **9** 18624

Katavouta A and Williams R G 2021 Ocean carbon cycle feedbacks in CMIP6 models: Contributions from different basins *Biogeosciences* **18** 3189–218

Keller K M, Joos F and Raible C C 2014 Time of emergence of trends in ocean biogeochemistry *Biogeosciences* **11** 3647–59

Khatiwala S *et al* 2013 Global ocean storage of anthropogenic carbon *Biogeosciences* **10** 2169–91

Koven C D *et al* 2022 Multi-century dynamics of the climate and carbon cycle under both high and net negative emissions scenarios *Earth Syst. Dyn.* **13** 885–909

Landschützer P, Gruber N, and Bakker D C E 2020 An observation-based global monthly gridded sea surface pCO2 and air-sea CO2 flux product from 1982 onward and its monthly climatology (NCEI Accession 0160558). Version 6.6 (NOAA National Centers for Environmental Information) (available at: https://doi.org/10.7289/v5z899n6) (Accessed 12 July 2022)

Landschützer P, Gruber N, Bakker D C E, Stemmler I and Six K D 2018 Strengthening seasonal marine CO2 variations due to increasing atmospheric CO2 *Nat. Clim. Change* **8** 146–50

Lei M, Hurtt G C, Chini L P, Sahajpal R, Pongratz J, Frolking S, Stehfest E, Klein Goldewijk K, O'Leary D and Doelman J C 2020 Global rules for translating land-use change (LUH2) to land-cover change for CMIP6 using GLM2 *Geosci. Model Dev.* **13** 3203–20

Lovenduski N S, Gruber N, Doney S C and Lima I D 2007 Enhanced CO2 outgassing in the Southern Ocean from a positive phase of the Southern Annular Mode *Glob. Biogeochem. Cycles* **21** GB2026

McKinley G A, Pilcher D J, Fay A R, Lindsay K, Long M C and Lovenduski N S 2016 Timescales for detection of trends in the ocean carbon sink *Nature* **530** 469–72

Meinshausen M *et al* 2020 The shared socio-economic pathway (SSP) greenhouse gas concentrations and their extensions to 2500 *Geosci. Model Dev.* **13** 3571–605

Mikaloff Fletcher S E *et al* 2006 Inverse estimates of anthropogenic CO2 uptake, transport and storage by the ocean *Glob. Biogeochem. Cycles* **20** GB2002

Mora C *et al* 2013 The projected timing of climate departure from recent variability *Nature* **502** 183–7

Nakano H, Ishii M, Rodgers K B, Tsujino H and Yamanaka G 2015 Anthropogenic CO2 uptake, transport, storage and dynamical controls in the ocean imposed by the meridional overturning circulation: a modeling study *Glob. Biogeochem. Cycles* **29** 1706–24

Notz D and Community S 2020 Arctic Sea Ice in CMIP6 *Geophys. Res. Lett.* **47** e2019GL086749

O'Neill B C *et al* 2016 The Scenario Model Intercomparison Project (ScenarioMIP) for CMIP6 *Geosci. Model Dev.* **9** 3461–82

Olonscheck D, Rugenstein M and Marotzke J 2020 Broad consistency between observed and simulated trends in sea surface temperature patterns *Geophys. Res. Lett.* **47** e2019GL086773

Ridge S M and McKinley G A 2020 Advective controls on the north atlantic anthropogenic carbon sink *Glob. Biogeochem. Cycles* **34** 1–17

Rodgers K B, Lin J and Frölicher T L 2015 Emergence of multiple ocean ecosystem drivers in a large ensemble suite with an Earth System Model *Biogeosciences* **12** 3301–20

Rodgers K B, Schlunegger S, Slater R D, Ishii M, Frölicher T L, Toyama K, Plancherel Y, Aumont O and Fassbender A J 2020 Reemergence of anthropogenic carbon into the ocean's mixed layer strongly amplifies transient climate sensitivity *Geophys. Res. Lett.* **47** e2020GL089275

Roy T, Bopp L, Gehlen M, Birgit Schneider P C, Frölicher T L, Segschneider J, Jerry Tjiputra C H and Joos F 2011 Regional impacts of climate change and atmospheric CO2 on future ocean carbon uptake: a multimodel linear feedback analysis *J. Clim.* **24** 2300–18

Sabine C L *et al* 2004 The oceanic sink for anthropogenic CO2 *Science* **305** 367–71

Sabine C L and Tanhua T 2010 Estimation of anthropogenic CO2 inventories in the ocean *Annu. Rev. Marine Sci.* **2** 175–98

Sarmiento J L and Gruber N 2006 *Ocean Biogeochemical Dynamics* (Princeton University Press)

Schlunegger S, Rodgers K B, Sarmiento J L, Frölicher T L, Dunne J P, Ishii M and Slater R 2019 Emergence of anthropogenic signals in the ocean carbon cycle *Nat. Clim. Change* **9** 719–25

Schwinger J and Tjiputra J 2018 Ocean carbon cycle feedbacks under negative emissions *Geophys. Res. Lett.* **45** 5062–70

Seland O *et al* 2020a NorESM2 source code as used for CMIP6 simulations *Zenodo*

Seland O *et al* 2020b Overview of the Norwegian Earth System Model (NorESM2) and key climate response of CMIP6 DECK, historical and scenario simulations *Geosci. Model Dev.* **13** 6165–200

Takahashi T, Olafsson J, Goddard J G, Chipman D W and Sutherland S C 1993 Seasonal variation of CO2 and nutrients in the high-latitude surface oceans: a comparative study *Glob. Biogeochem. Cycles* **7** 843–78

Tjiputra J F, Assmann K and Heinze C 2010 Anthropogenic carbon dynamics in the changing ocean *Ocean Sci.* **6** 605–14

Tjiputra J F, Negrel J and Olsen A 2023 Early detection of anthropogenic climate change signals in the ocean interior *Sci. Rep.* **13** 3006

Tjiputra J F, Olsen A, Bopp L, Lenton A, Pfeil B, Roy T, Segschneider J, Totterdell I and Heinze C 2014 Long-term

surface pCO$_2$ trends from observations and models *Tellus* B **66** 23083

Tjiputra J and Gupta A K 2023 What goes in must come out: the oceanic outgassing of anthropogenic carbon: simulations outputs [Dataset] *Zenodo* https://doi.org/10.5281/zenodo.10027151

Toyama K, Rodgers K B, Blanke B, Iudicone D, Ishii M, Aumont O and Sarmiento J L 2017 Large reemergence of anthropogenic carbon into the ocean's surface mixed layer sustained by the ocean's overturning circulation *J. Clim.* **30** 8615–31

Wanninkhof R 2014 Relationship between wind speed and gas exchange over the ocean revisited *Limnol. Oceanogr. Methods* **12** 351–62

Wetzel P, Winguth A and Maier-Reimer E 2005 Sea-to-air CO2 flux from 1948 to 2003: a model study *Glob. Biogeochem. Cycles* **19** GB2005

Zhai P, Rodgers K B, Griffies S M, Slater R D, Iudicone D, Sarmiento J L and Resplandy L 2017 Mechanistic drivers of reemergence of anthropogenic carbon in the equatorial Pacific *Geophys. Res. Lett.* **44** 9433–9